

# Computational super-resolution phase retrieval from multiple phase-coded diffraction patterns: simulation study and experiments

VLADIMIR KATKOVNIK<sup>1</sup>, IGOR SHEVKUNOV<sup>1,2,\*</sup>, NIKOLAY V. PETROV<sup>2</sup>, AND KAREN EGIAZARIAN<sup>1</sup>

<sup>1</sup>Laboratory of Signal Processing, Tampere University of Technology, P.O. Box 553 FI-33101 Tampere, Finland

<sup>2</sup>Department of Photonics and Optical Information Technology, ITMO University, St. Petersburg, Russia

\*Corresponding author: Igor.shevkunov@tut.fi

Compiled April 10, 2017

Computational super-resolution inverse diffraction phase retrieval is considered. The optical setup is lensless with a spatial light modulator (SLM) for aperture phase coding. The paper is focused on experimental tests of the Super-Resolution Sparse Phase Amplitude Retrieval (SR-SPAR) algorithm. We start from simulation tests and go to physical experiments. Both simulation tests and experiments demonstrate a good quality imaging for super-resolution with the factor 4, which means that the computational pixels of the reconstructed object are 4 times smaller than the sensor pixels. © 2016 Optical Society of America

**OCIS codes:** (100.6640) Superresolution, (100.5070) Phase retrieval, (100.0100) Image processing, (110.4280) Noise in imaging systems, (070.2025) Discrete optical signal processing.

<http://dx.doi.org/10.1364/optica.XX.XXXXXX>

## 1. INTRODUCTION

### A. Problem setup

The phase retrieval problem concerns reconstruction of 2D and 3D complex-domain objects provided that only intensity of light radiation is measured. Such problems appear in science and engineering with a wide area of applications from astronomy and optics to medicine and biology (e.g. [1–3]).

The standard formalization of the phase retrieval problem is of the form:

$$y_s = |\mathcal{P}_s\{u_o\}|^2, s = 1, \dots, L, \quad (1)$$

where:  $u_o \in \mathbb{C}^{N \times N}$  is an  $N \times N$  complex-valued 2D image of object (specimen);  $\mathcal{P}_s: \mathbb{C}^{N \times N} \mapsto \mathbb{C}^{M \times M}$  is a complex-valued forward propagation operator from object to sensor planes,  $y_s \in \mathbb{R}_+^{M \times M}$  are  $M \times M$  intensity measurements at the sensor plane,  $L$  is a number of experiments, and  $u_s = \mathcal{P}_s\{u_o\}$  is a notation for the complex-valued wavefront at the sensor plane.

In this paper we consider the setup with the aperture modulation such that

$$u_s = \mathcal{P}_s\{u_o\} = \mathcal{P}\{\mathcal{M}_s \circ u_o\}. \quad (2)$$

Here  $\mathcal{M}_s \in \mathbb{C}^{N \times N}$  are phase modulation masks,  $\mathcal{M}_s(k, l) = \exp(j\phi_{k,l}(s))$ , and the 'o' stands for the entry-wise (Hadamard) product of two matrices.

The phases  $\phi_{k,l}(s)$  in  $\mathcal{M}_s$  can be generated as deterministic or random. It results in the observations known as *coded diffraction patterns* (e.g. [4]):

$$y_s = |\mathcal{P}\{\mathcal{M}_s \circ u_o\}|^2, s = 1, \dots, L. \quad (3)$$

The phase modulation is able to change dramatically the diffraction pattern of  $\mathcal{P}\{u_o\}$  enabling redistribution of observed intensities from low to higher frequencies.

Various methods are developed in order to make these  $\mathcal{P}_s$  sufficiently different in order to gain *observation diversity* enabling finding  $u_o$  from observations  $\{y_s\}_1^L$ . A defocussing of the registered images is one of the instruments to get a sufficient phase diversity [5–9]. In the recent development a spatial light modulator (SLM) is exploited for the defocussing (e.g. [10, 11]).

A modulation of the wavefront is another efficient tool to achieve the desirable diversity of observations (e.g. [12–14]).

For noisy observations Eq. (3) is changed for

$$z_s = \mathcal{G}\{|u_s|^2\}, s = 1, \dots, L, \quad (4)$$

where  $\mathcal{G}$  stands for a generator of random observations.

For the wavefront propagation from the object to the sensor plane we use the Rayleigh-Sommerfeld model with the transfer function defined through the angular spectrum (AS) ([15], Eq. (3-74)):

$$u_s(x, y, z) = \mathcal{F}^{-1} \left[ H(f_x, f_y, z) \cdot \mathcal{F}[u_s(x, y, 0)] \right] \quad (5)$$

$$H(f_x, f_y, z) = \begin{cases} \exp \left[ i \frac{2\pi}{\lambda} z \sqrt{1 - \lambda^2 (f_x^2 + f_y^2)} \right], & f_x^2 + f_y^2 \leq \frac{1}{\lambda^2}, \\ 0, & \text{otherwise,} \end{cases} \quad (6)$$

where the operators  $\mathcal{F}$  and  $\mathcal{F}^{-1}$  stay for the Fourier transform (FT) and inverse Fourier transforms, respectively;  $u_s(x, y, z)$  is a wavefront propagated on the distance  $z$  from the initial position  $u_s(x, y, 0)$ ;  $H(f_x, f_y, z)$  is the angular spectrum transfer function;  $f_x, f_y$  are spatial frequencies;  $x, y$  denote spatial coordinates, and  $\lambda$  is the wavelength.

In this paper we assume that the observations have Poissonian distribution typical for optical photon counting. This process is well modelled by independent Poissonian random variables in the form

$$p(z_s[l] = k) = \exp(-y_s[l]\chi) \frac{(y_s[l]\chi)^k}{k!}, \quad (7)$$

where  $p(z_s[l] = k)$  is a probability that the random observation  $z_s[l]$  takes integer value  $k \geq 0$  and  $y_s[l]$  is the intensity of the wavefront, defined by Eq. (1), at the pixel  $l$ .

The parameter  $\chi > 0$  in Eq. (7) is a scaling factor of the Poisson distribution. Defining the observation signal-to-noise ratio (SNR) as the ratio between the square of the mean and the variance of  $z_s$ , we have  $SNR = E^2\{z_s\}/\text{var}\{z_s\} = y_s\chi$ . It follows, that the relative noisiness of observations becomes stronger as  $\chi \rightarrow 0$  ( $SNR \rightarrow 0$ ) and approaches zero when  $\chi \rightarrow \infty$  ( $SNR \rightarrow \infty$ ). The latter case corresponds to the noiseless scenario, i.e.  $z_s/\chi \rightarrow y_s$  with probability 1. The scale parameter  $\chi$  is of importance for modeling as it allows to control a level of noise in observations.

Reconstruction of the complex-valued object  $u_o$  (phase and amplitude) from noiseless or noisy observations is *phase retrieval problem*. Here *phase* emphasizes, that in the object the phase is a variable of the first priority, while the amplitude may be an auxiliary variable often useful only in order to improve the phase imaging.

## B. Phase retrieval algorithms

There is a flow of publications on the phase retrieval. Various versions of the Gerchberg-Saxton (GS) technique are quite universal for different setups (e.g. [7–9, 16, 17]). These algorithms based on alternating projections between the object and observations planes are flexible in order to incorporate any information available for variables in these planes. Recent developments in this area as well as the review can be seen in [18].

Contrary to this type intuitive heuristic algorithms the variational formulations have a stronger mathematical background and based on numerical algorithms solving some optimization problems (e.g. [19–21]).

A new variational algorithm for the phase retrieval from noisy data based on *transform domain sparsity* for the object phase and amplitude is developed in [22]. The sparsity concept as a tool for phase retrieval is a topic of the paper [23], where the original sparsifying learning transform is developed.

The phase retrieval from coded diffraction patterns is of special interest in the recent publications (e.g. [13, 24]). The uniqueness of the phase retrieval in this scenario is proved in the later paper.

The spatial resolution of phase retrieval is limited by two factors: low-pass filtering by the propagation operator  $\mathcal{P}$  and the size of sensor's pixels. High-frequency spatial information is lost in intensity observations, which can be treated as corresponding to a sub-sampled true object  $u_o$ . The super-resolution imaging allows to compensate this sub-sampling effect.

One of the straightforward approaches to overcome the pixel size limitations is to use a sequence of laterally shifted holograms (e.g. [25–27]).

The computational approach to the super-resolution is different assuming that the optical setup is fixed and the super-resolution image should be extracted from the data available. Note, that for the real-domain the computational imaging is a hot topic with a flow of publication, while for the complex-domain, phase/amplitude imaging, the situation is quite different actually with a few publications, which can be referred, in particular, for phase retrieval.

Compressed sensing (CS) is one of the comparatively new computational techniques for restoration of sub-sampled data. Application of this sort of the techniques in optics can be found in [28, 29]. CS can be treated as a super-resolution, however, there is a deep difference between these two problems. CS is focused on the sub-sampling design with the smallest number of observations as a target, while in the super-resolution the observations are given on a usually regular and fixed grid.

## C. Contribution and structure of this paper

The transform domain phase/amplitude sparsity introduced in [22] was generalized for the super-resolution phase retrieval in [30]. In this paper we modify this algorithm for the lensless optical setup with the AS transfer function for wavefront propagation, Eqs. (5-6). Contrary to it, the lenslet and FT propagation model are used in [30]. We provide simulation test and experimental results demonstrating that the proposed algorithm enables the super-resolution phase-retrieval with the up-sampling factor upto 4.

In what follows the proposed algorithm is presented in Section 2. The experiment's details and results are discussed in Section 3.

## 2. SUPER-RESOLUTION PHASE RETRIEVAL

### A. Complex domain sparsity

The complex domain sparsity for the object as it is used in this paper assumes that there are small fragments (patches) of the object  $u_o$ , which have similar features. These similar patches can be found in different parts of the image. It follows that these patches taken together admit *sparse* representations: they can be well approximated by linear combinations of a small number of basic functions.

The complex domain images, such as the object  $u_o = B_o \exp(i\varphi_o)$ , are defined by two variables: phase  $\varphi_o$  and amplitude  $B_o$ . Respectively, the sparse representation can be imposed on the following pairs of the real-valued variables:

- (1) The phase  $\varphi$  (interferometric or absolute) and the amplitude  $B_o$ ;
- (2) The real and imaginary parts of  $u_o$ .

In this paper we apply the absolute phase/amplitude sparsity following to [31, 32], where it has been already tested for various optical problems.

The success of the sparsity approach depends on how reach and redundant are dictionaries (sets of basic functions) used for image analysis and synthesis. In this paper for the sparsity implementation we use the Block-Matching and 3D filtering (BM3D) algorithm [33].

Let us mention basic steps of this advanced technique known as *nonlocal self-similarity sparsity*. At the first stage the image is partitioned into small overlapping square patches. For each patch a group of similar patches is collected which are stacked together to form a 3D array (group). This stage is called *grouping*. The entire 3D group-array is projected onto a 3D predefined transform basis. The spectral coefficients obtained as a result of this transform are hard-thresholded (small coefficients are zeroed) and the inverse 3D transform gives the filtered patches, which are returned to the original position of these patches in the image. This stage is called *collaborative filtering*. This process is repeated for all pixels of the entire image and obtained overlapped filtered patches are aggregated in the final image estimate. This last stage is called *aggregation*. The details of this algorithm can be seen in [33].

The links of this algorithm with the general sparsity concept are revealed in [34]. It is shown that the *grouping* operations result in data adaptive analysis and synthesis image transforms (frames), which combined with the hard-thresholding of these transforms define the BM3D algorithm. It is emphasized that the sparsity is achieved mainly due to the grouping which allows to analysis jointly similar patched and this way to guaranty the sparsity (self-similarity of patches) at least for each of the 3D groups.

Note, that the standard BM3D algorithm as it is presented in the [33] is composed from two successive steps: thresholding and Wiener filtering. In this paper we use a simplified version of BM3D including grouping, transforms and thresholding without Wiener filtering. In this form this algorithm is obtained from the variational setting of the wavefront retrieval problem.

It is shown in [22] that the nonlocal block-wise sparsity imposed on phase and amplitude results in the separate BM3D filtering of phase and amplitude

$$\hat{\varphi}_o = BM3D_{phase}(\varphi_o, th_\varphi), \quad (8)$$

$$\hat{B}_o = BM3D_{ampl}(B_o, th_B). \quad (9)$$

Here  $\hat{\varphi}_o$  and  $\hat{B}_o$  are sparse approximations of  $\varphi_o$  and  $B_o$ ; *phase* and *ampl* as indices of BM3D are used in order to emphasize that the parameters of BM3D can be different for the phase and amplitude;  $th_\varphi$  and  $th_B$  are thresholding parameters of the algorithms. The phase in Eq. (8) can be interferometric or absolute depending on the sparsity formulation.

## B. Super-resolution SPAR algorithm

Conventionally the pixels are square  $\Delta_{SLM} \times \Delta_{SLM}$  and  $\Delta_S \times \Delta_S$  for SLM and sensor, respectively. A continuous object is discretized by *computational* pixels  $\Delta_c \times \Delta_c$ . This discretization is necessary both for digital data processing as well as for modeling of wavefront propagation and image formation. Contrary to the pixels of SLM and sensor defined by the corresponding optical-electronic devices the object pixels  $\Delta_o$  are computational, which maybe be taken of arbitrary small sizes.

Assuming for a moment  $\Delta_c = \Delta_S$ , reconstruction of  $u_o$  from the observations  $\{z_s\}$  is the conventional phase retrieval with

the resolution for the object dictated by the pixel size of the sensor. Let us term this case *pixel-resolution* imaging.

If  $\Delta_c < \Delta_S$  we arrive to a much more interesting problem of *pixel super-resolution*. It is convenient to assume that  $\Delta_S = r_s \cdot \Delta_c$ , where  $r_s \geq 1$  is an integer pixel super-resolution (up-sampling) factor, and  $\Delta_{SLM} = r_{SLM} \cdot \Delta_c$ ,  $r_{SLM} \geq 1$ , where  $r_{SLM}^2$  is a number of smaller  $\Delta_c \times \Delta_c$  computational object pixels covering a single SLM pixel. This SLM pixel gives the same modulation phase-shift for all object pixels in this group.

In order to study the various effects of SLM phase modulation, we introduce an SLM super-pixel as a larger size pixel  $M \cdot \Delta_{SLM} \times M \cdot \Delta_{SLM}$ , which is composed from adjacent  $M \times M$  SLM's pixels. In the phase modulation, all corresponding  $M \times M$  SLM's pixels provide for modulation the same phase shift.

The computational wavefront reconstruction is going from the continuous domain wavefront propagation Eqs. (5-6) to the corresponding discrete model based on pixelation of the object distribution  $u_o$ , thus, we arrive to the discrete modeling of the system at hand linking the discrete values of sensor output (observations) with the discrete values of the object, where the integral FT is replaced by Fast Fourier Transform (FFT). Note, that all these calculations are produced for the variables given with the computation sampling period  $\Delta_c$ .

It is well known, that a discrete modelling of the continuous propagation model Eqs. (5-6) imposes the restrictions on the computational sampling period  $\Delta_c$  with connection to the distance  $z$ , the wavelength  $\lambda$  and the computational aperture size. With the reference to [35], [36] and [37], for the considered scenario, these restrictions can be given as the inequality

$$z \leq z_{\max} = N\Delta_c^2/\lambda, \quad (10)$$

where  $z_{\max}$  is an upper bound for the distance between the object and sensor, and  $N$  defines the  $N \times N$  computational support of zeropadded object and sensor, with the computational apertures size  $N\Delta_c \times N\Delta_c$ .

In order to simplify the algorithm presentation we preserve the notation  $\mathcal{P}$  for this discrete model initially introduced for the continuous variables and integrals. Then the algorithm can be given in the form similar to the phase retrieval super-resolution algorithm in [30]. We use the abbreviation SR-SPAR (Super-Resolution Sparse Phase Amplitude Retrieval) for this algorithm.

It is important to note that SR-SPAR is originated from the variational formulation introduced for optimal reconstruction of  $u_o$  from Poissonian observations  $\{z_s[k, l]\}$ . The corresponding minus log-likelihood for Poissonian observations according to Eq. (7) is as follows

$$\mathcal{L} = \sum_{s=1}^L \sum_{k,l} [ |u_s[k, l]|^2 \chi - z_s[k, l] \log(|u_s[k, l]|^2 \chi) ]. \quad (11)$$

This criterion should be minimized with respect to  $u_o[k, l]$  provided the equations linking  $u_o$  and  $u_s$  and restrictions imposed by the sparsity requirements.

The derivation of the algorithm is similar to the technique developed in [22] for the pixel-resolution phase retrieval and the FT propagation. The difference mainly concerns the used propagation operator and the sampling rates, which are  $\Delta_o = \Delta_S$  in [22] and  $\Delta_o = \Delta_S/r_s$  in this paper, then the observations should be upsampled with the factor  $r_s$ .

We show the block-scheme of this algorithm in Fig. 1 referring to [22] and [30].

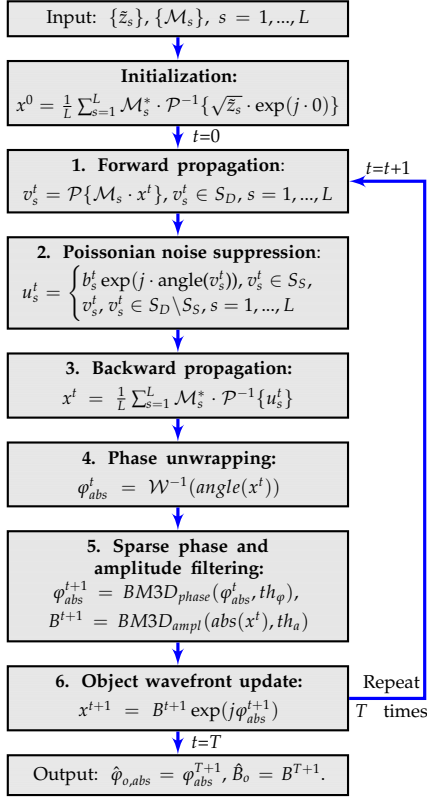


Fig. 1. SR-SPAR algorithm.

The inputs  $\tilde{z}_s$  in this algorithm are upsampled by factor  $r_s$  observations  $z_s$ . We use the zero-order upsampling giving  $\tilde{z}_s$  as piece-wise invariant with the invariant values for computational pixels corresponding to each of the larger size pixels of the sensor. At the initialization step the initial estimate of the object wavefront  $x^0$  is created. At Step 1 the object wavefront estimate  $x^t$  is multiplied by the phase mask  $\mathcal{M}_s$  and propagates using the operator  $\mathcal{P}$  to the sensor plane, the result is denoted as  $v_s^t$ . These wavefronts are calculated for the computational diffraction area  $N \times N$  denoted  $S_D$ .

At Step 2 this wavefront is updated to the variable  $u_s^t$  by filtering the amplitude of  $v_s^t$  according to the given observations  $\tilde{z}_s$ . The following formula as derived in [22] defines the rule how the amplitude  $b_s$  is calculated:

$$b_s = \frac{|v_s| + \sqrt{|v_s|^2 + 4\tilde{z}_s\gamma(1 + \gamma_1\chi)}}{2(1 + \gamma_1\chi)}. \quad (12)$$

These calculations are element wise;  $\gamma_1 > 0$  is the parameter of the algorithm. Naturally, this update is produced provided known observation  $\tilde{z}_s$ , i.e. for the pixels belonging to the sensor area  $S_S$ ,  $v_s \in S_S$ . In our modeling the computational diffraction area is always equal or larger than the sensor area,  $S_S \subset S_D$ . For the area out of the sensor the wavefront values are preserved,  $u_s = v_s$  for  $v_s \in S_D \setminus S_S$ .

At Step 3 the estimates  $\{u_s^t\}$  backpropagate to the object plane and update the object wavefront estimate  $x^{t+1}$ . Here  $\mathcal{M}_s^*$  means a complex conjugate  $\mathcal{M}_s$  and  $\mathcal{P}^{-1}\{u_s^t\}$  means inverse of the model Eq. (5).

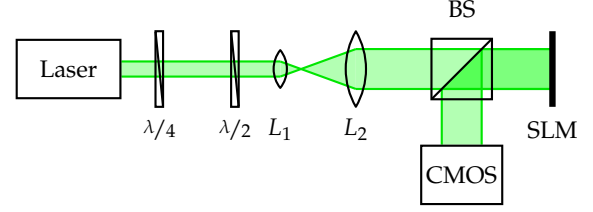


Fig. 2. Optical setup.  $\lambda/4, \lambda/4$  –retardation plates,  $L_1, L_2$  – lenses, BS – beamsplitter, SLM – Spatial Light Modulator, CMOS – registration camera.

The unwrapping of the phase with reconstruction of absolute phase in Step 4 is necessary only if the object phase range goes beyond  $2\pi$  [38]. The sparsification (filtering on the base of sparse approximations) is produced in Step 5. At step 6 the final iteration estimation is obtained.

The SR-SPAR algorithm is based on the phase retrieval algorithm derived by solving the optimization problem for the phase retrieval from Poissonian observations. The formalization and techniques used in [22] are completely applicable with small modifications for derivation of SR-SPAR. Thus, the presented SR-SPAR algorithm is designed as optimal one for Poissonian observations.

### C. Parameters of the SR-SPAR algorithm

The performance of the SR-SPAR algorithm essentially depends on its parameters. Optimization can be produced for each amplitude/phase distribution and the noise level. However, in our experiments the parameters are fixed for all our experiments. The image patches in  $BM3D$  are square  $3 \times 3$ . The group size is limited by 39 patches. The step size between the neighbouring patches is equal to 2. The discrete cosine (for patches) and Haar (for the group length) transforms are used for 3D group data processing in  $BM3D$ .

The parameters defining the iterations of the algorithm are as follows:  $\gamma_1 = 1/\chi$ ;  $th_a = 2.0$ ;  $th_\phi = 2.0$ . The number of the iterations is fixed to 30.

For our experiments we use MATLAB R2016b and the computer with the processor Intel(R) Core(TM) i7-3770 CPU @ 3.40 GHz, 32 Gb RAM.

The computation complexity of the algorithm is characterized by the time required for processing. For 30 iterations,  $L = 10$  and  $64 \times 64$  images, zero-padded to  $4992 \times 4992$ , this time is equal 2150 sec.

We make publicly available the MATLAB demo-codes <http://www.cs.tut.fi/sgn/imaging/sparse> of the developed SR-SPAR algorithm, which can be used to reproduce the experiments presented in this paper as well as for further tests.

## 3. RESULTS AND DISCUSSION

### A. Experimental setup

Experimental setup is presented in Fig. 2: laser LASOS GLK 3250 TS with wavelength  $\lambda = 532$  nm, digital 8-bit CMOS camera EVS 3264  $\times$  2448 with pixel size  $\Delta_S = 1.4 \mu\text{m}$ , phase only reflective Spatial Light Modulator (SLM) Holoeye LETO 1920  $\times$  1080 with pixel size  $\Delta_{SLM} = 6.4 \mu\text{m}$  and fill factor 93% were utilized. Light beam emitted by the laser source changes

its vertical polarization to horizontal in a system of two retardation plates  $\lambda/4$  and  $\lambda/2$ , next, beam expands in two lenses  $L_1$  and  $L_2$  collimator and goes through the beamsplitter (BS) to the SLM, where light wavefront obtains desired phase retardation and propagates to the CMOS camera through the same beamsplitter BS. Optical distance between SLM and CMOS is equal 21.55 mm. In our system the phase object was modelled on the SLM. It is assumed in this case that we can exactly know its phase distribution. The developed algorithm has been tested in numerical experiments on two phase objects with invariant amplitude,  $B_0 = 10$ , and phase images "cameraman" and logo "TUT", see Figs. 3–4, middle images in the top rows.

In our experiments both the phase object and phase modulation masks are implemented on SLM. Thus, the object's pixels size is equal to SLM's pixel size,  $\Delta_o = \Delta_{SLM}$ . The size of the object in pixels is  $64 \times 64$  pixels (SLM's pixels). In modelling we use the parameters corresponding to the ones used in physical experiments: propagation distance  $z = 21.55$  mm,  $\Delta_S = 1.4$   $\mu\text{m}$ ,  $\Delta_{SLM} = 4 \times \Delta_S$ ,  $\Delta_o = \Delta_{SLM}$ .

Our objects and sensor are zero-padded to  $4992 \times 4992$  pixels, i.e.  $N = 4992$ . It is the largest dimension allowed by RAM of our computer. We produced experiments with the super-resolution factor  $r_s = 1, 2, 3, 4$ . In what follows we show the results only for  $r_s = 1$  (pixel resolution) and  $r_s = 4$  (sub-pixel resolution), then the computational pixels are of the size from  $\Delta_c = 1.4$   $\mu\text{m}$  to  $\Delta_c = 0.35$   $\mu\text{m}$ .

The propagation distance  $z = 21.55$  mm is minimal for our optical setup restricted by the used reflective SLM. For  $r_s = 1$  the distance  $z_{\text{max}}$  in Eq. (10) is  $z_{\text{max}} = 18.4$  mm. This upper bound is smaller than the used distance  $z = 21.55$  mm but the difference between these parameters is not large. Thus, we can assume that at least for the pixel resolution the theoretical requirement (Eq. (10)) is approximately fulfilled.

## B. Simulation experiments

For simulation of the observations  $\tilde{z}_s$  we take the true phase image of the object  $64 \times 64$ , and assume that it is created on the SLM. Therefore its pixel size  $\Delta_o$  is equal to  $\Delta_{SLM}$ . As long as our computational pixels  $\Delta_c$  are smaller than  $\Delta_{SLM}$ , we do phase object upsampling by a factor  $r_{SLM} = \Delta_{SLM}/\Delta_c$ . Next we do zero-padding of this upsampled object and add phase masks  $\mathcal{M}_s$  to its phase. Next these wavefronts are propagated to the CMOS camera, and squared absolute values of the propagation results are observations  $\tilde{z}_s$ , which correspond to pixels size  $\Delta_c$ . To get realistic observations we average intensities of joint pixels in areas  $r_s \times r_s$  on whole surface of the  $\tilde{z}_s$ , where  $r_s = \Delta_s/\Delta_c$ , as a result we have  $\Delta_s$ -wise observations  $\tilde{z}_s$ .

In what follows we show the results for nearly noiseless observations with the Poissonian scale parameter  $\chi = 1000$ . Demonstration of how the SPAR algorithm suppresses the Poissonian noise can be seen in [22], where it is done for the pixel resolution and FT propagation model. Similar strong filtering can be demonstrated for the super-resolution by SR-SPAR.

### B.1. Pixel resolution

In Figs. 3–4 we present results for the *pixel-resolution* case, i.e. the computational and sensor pixels have equal sizes:  $\Delta_c = \Delta_s$ ,  $\Delta_o = \Delta_{SLM}$ , and  $\Delta_{SLM} = 4 \cdot \Delta_s$ ,  $M = 8$ . The later means that for masks we use the SLM's superpixel with  $M = 8$ .

It follows from the figures, that SR-SPAR demonstrates perfect results in phase reconstruction and negligible errors in amplitude reconstructions. We can note also that the amplitude errors are definitely connected with the phase variations. The am-

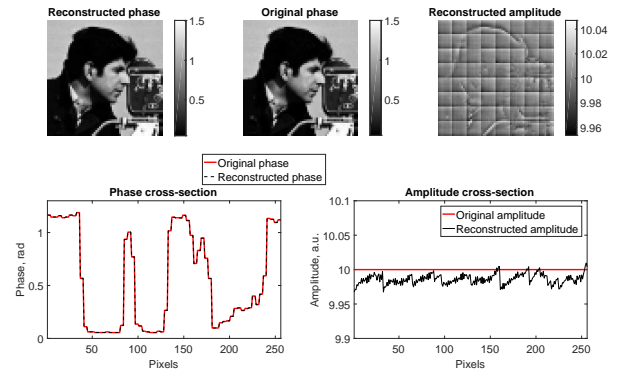


**Fig. 3.** Reconstructions for simulated phase image "cameraman", *pixel-resolution*,  $r_s = 1$ . Top line: phases reconstructed and original, left and middle images, respectively, and reconstructed amplitude –right image. Bottom line - phase (left) and amplitude (right) longitudinal cross-sections.  $RMSE_{\text{phase}} = 0.00253$ .

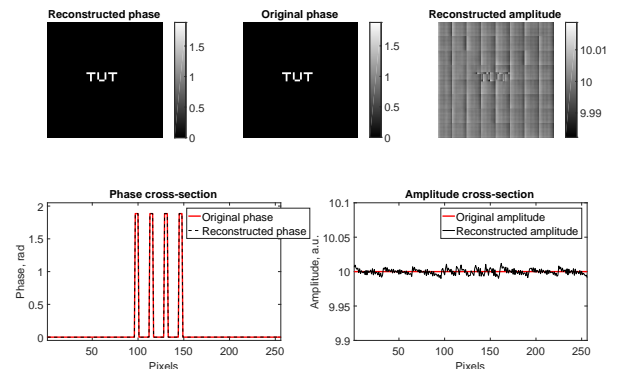


**Fig. 4.** Reconstructions for simulated phase image logo "TUT", *pixel-resolution*,  $r_s = 1$ . Top line: reconstructed and original, left and middle images, respectively, and reconstructed amplitude –right image. Bottom line - phase (left) and amplitude (right) longitudinal cross-sections.  $RMSE_{\text{phase}} = 0.000852$ .

plitude reconstructions have clear seen squares forming  $8 \times 8$  grids. These squares are mapping of the SLM's superpixel. Each of these squares has a size  $8 \times 8$  SLM's pixels. Thus, the total object size is  $64 \times 64$  in SLM's pixels and  $256 \times 256$  in the computational pixels  $\Delta_c$ .

In order to optimize the accuracy of reconstructions, we studied dependence of Root-Mean-Square Error (RMSE) with respect to the following four parameters: number of observations  $L$ , number of iterations  $T$ , standard deviation of the random phase in the phase modulation masks and size of the SLM's superpixel  $M$ . In the following we show these results calculated for the phase reconstructions and for the cameraman phase test-image only.

More or less similar results have been observed for "TUT" phase test-images and various values of the super-resolution factor  $r_s$ .

The dependence on the number of observations is presented in Fig. 5. It is a decreasing function taking a steady-state value starting from  $L = 10$ . We take this value of  $L$  for our simulation.

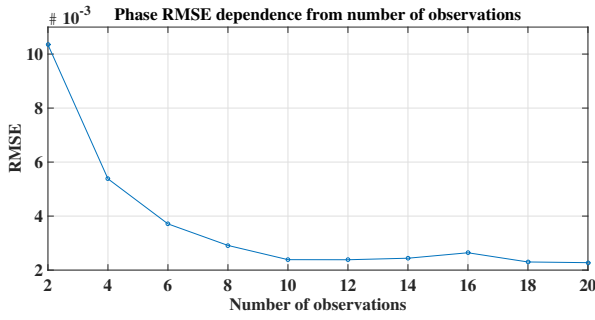


**Fig. 5.** Phase RMSE dependence from number of observations  $L$ .

However, for processing of experimental data we take a larger value  $L = 20$ .

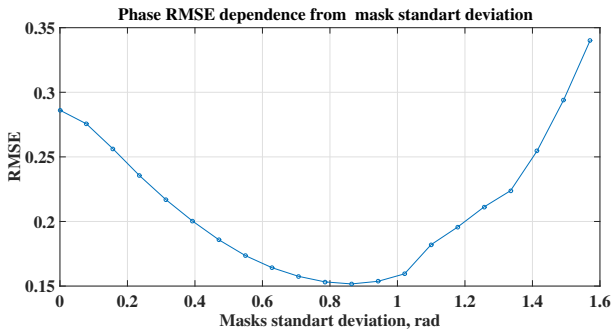


**Fig. 6.** Phase RMSE dependence from standard deviation of zero-mean Gaussian random mask.

The standard deviation ( $STD$ ) of the random zero-mean Gaussian phase masks is a crucial parameter for reconstruction because it influences both the accuracy and converges of the algorithm. Figure 6 illustrates RMSE as a function of  $STD$ . The curve takes a minimal value at  $STD = 0.3\pi$ , accepted for our experiments.

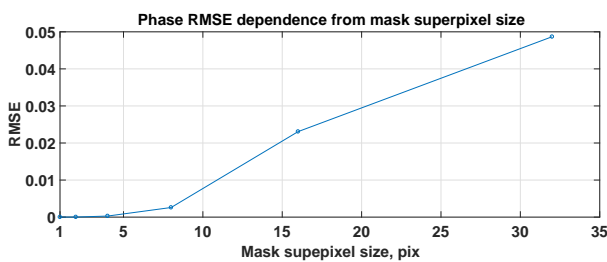


**Fig. 7.** Phase RMSE dependence from SLMs superpixel size  $M$ .

Another significant parameter is the SLM superpixel size  $M$ . Figure 7 clearly indicates that the best value is  $M = 1$ . We accept  $M = 1$  for simulation tests. However, it was observed that for processing of experimental data the larger value of  $M$  provides better results, we take  $M = 8$ . It happens due to the cross-talk effects between the adjacent SLM pixels [39]. As it is seen from Fig. 7  $M = 8$  does not seriously increase RMSE value as compared with  $M = 1$ .

Figure 8 illustrates the performance of the algorithm with

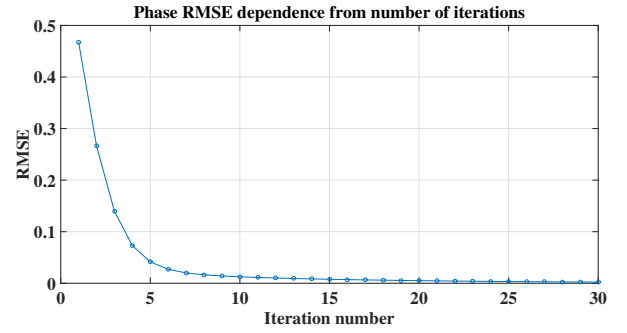


**Fig. 8.** Phase RMSE dependence from iteration number  $T$ .

respect to the iteration number  $T$ . The RMSE curve is monotonically decreasing with the steady state values achieved after about 15 iterations. Nevertheless, for experimental data we take  $T = 30$ .

## B.2. Subpixel super-resolution

In this subsection we show the results for super-resolution performance of SR-SPAR with the super-resolution factor  $r_s = 4$ , i.e.  $\Delta_S = r_s \cdot \Delta_c$ ,  $\Delta_{SLM} = 4 \cdot \Delta_S$ ,  $\Delta_o = \Delta_{SLM}$  and  $\Delta_c = 0.35 \mu\text{m}$ . This computational pixel value is smaller than the wavelength,  $\lambda = 532 \text{ nm}$ . In this way we arrive to the sub-wavelength resolution. Figures 9–10 demonstrate nearly perfect reconstructions, which are similar to the reconstructions obtained for the *pixel-resolution* case.

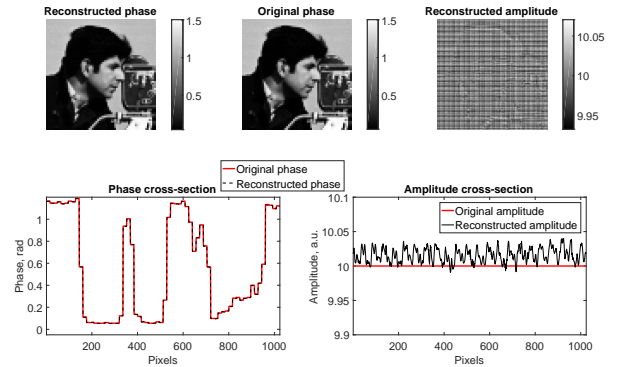


**Fig. 9.** Reconstructions for simulated cameraman phase image. *Subpixel super-resolution*,  $r_s = 4$ . Top line, reconstructed and original phase images, left and middle images, respectively, and reconstructed amplitude –right image. Bottom line – phase (left) and amplitude (right) longitudinal cross-sections.  $RMSE_{\text{phase}} = 0.00228$ .

## C. Physical experiments

The parameters used in the physical experiments are exactly correspond to those for simulation. The phase objects “cameraman” and “TUT” are modelled by SLM with the phase ranges  $[0, \frac{\pi}{5}]$  and  $[0, \frac{\pi}{6}]$ , respectively. The computational pixels have sizes  $\Delta_c = 1.4$  and  $0.35 \mu\text{m}$  for *pixel-* and *sub-pixel resolution*, respectively.

### C.1. Pixel resolution

The pixel-resolution images are shown in Figs. 11–12. Despite a large distance  $z$  between the object and sensor planes and, re-

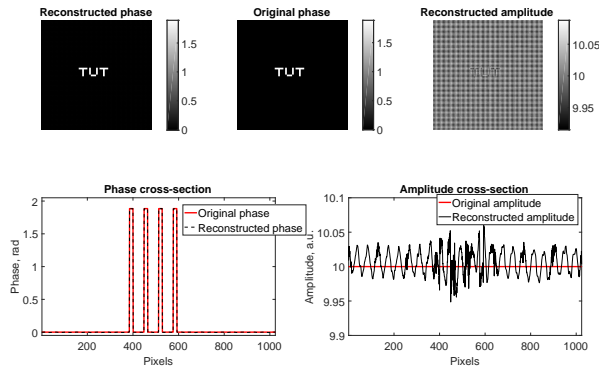


**Fig. 10.** Reconstructions for simulated phase image logo "TUT", *subpixel super-resolution*. Top line, phases: reconstructed and original, left and middle images, respectively, and reconstructed amplitude –right image. Bottom line - phase (left) and amplitude (right) longitudinal cross-sections.  $RMSE_{phase} = 0.000592$ .

spectively, strong diffraction effects in the registered holograms, SR-SPAR gives reliable results with well seen "cameraman" image in Fig. 11. The cameraman shape is also well seen in the amplitude reconstruction. It seems, that it happens due to a non-ideality of SLM with some leakage from phase to amplitude modulation. The corresponding phase cross-section demonstrates that the reconstruction follows the respective changes in the original image. The reconstructions for the "TUT" phase object are also quite acceptable as it is seen from the phase cross-section showing exactly to location of the peaks as well as their magnitudes. We can also see the features of the phase object in the amplitude reconstruction. Again at least partially, it can be addressed to the non-ideality of SLM. The blurred shape of the reconstructions as compared with the reconstructions obtained in the simulation tests is due to a quite approximate modeling of wavefront propagation imbedded in SR-SPAR and defined by Eqs. (5-6).

### C.2. Subpixel super-resolution

The results for *sub-pixel resolution* are presented in Figs. 13 – 14. Again we can see quite good reconstructions for both "cameraman" and "TUT" phase objects. The comments on amplitude reconstructions are identical to those given above for the pixel resolution case. It is interesting, that the subpixel super-resolution reconstructions look very similar to the reconstructions obtained for the pixel resolution. The only difference well seen in the cross-sections is that the *sub-pixel resolution* images are smoother than the pixel resolution ones. The blurred character of the reconstructions can be addressed to a quite approximate modeling of wavefront propagation by Eqs. (5-6).

For the super-resolution  $\Delta_c = \Delta_S/4$  and provided fixed  $N = 4992$ , the size of the image support in computational pixels,  $z_{max}$  in Eq. (10) takes value  $z_{max} = 18.4/16$  mm. It is much less than the used  $z = 21.55$  mm, thus the condition Eq. (10) is severely violated. It can be one of the cause of discrepancy between the reality and the model used for wavefront propagation.

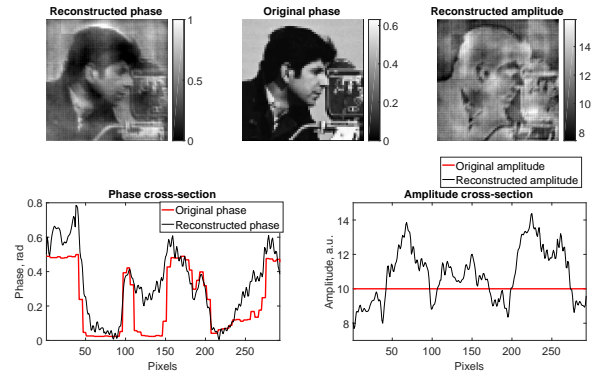


**Fig. 11.** Reconstructions for experimental data, phase object "cameraman", *pixel-resolution*. Top line, phases: reconstructed and original, left and middle images, respectively, and reconstructed amplitude –right image. Bottom line - phase (left) and amplitude (right) longitudinal cross-sections.

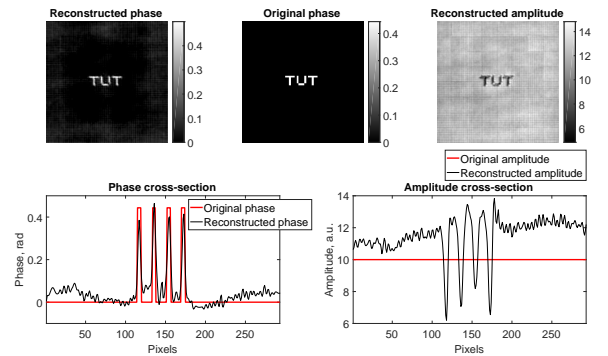


**Fig. 12.** Reconstructions for experimental data, phase object logo "TUT", *pixel-resolution*. Top line, phases: reconstructed and original, left and middle images, respectively, and reconstructed amplitude –right image. Bottom line - phase (left) and amplitude (right) longitudinal cross-sections.

## 4. CONCLUSION

Computational subpixel super-resolution phase retrieval is considered for phase-coded intensity observations. The iterative algorithm is proposed for the lensless setup with the scalar Rayleigh-Sommerfeld model for wavefront propagation. One of the essential instruments of the algorithm is a sparsity hypothesis applied to both phase and amplitude. The efficiency of the algorithm is confirmed by simulation tests and experiments. It is shown that the high level super-resolution can be achieved with the super-resolution factor up to 4, i.e. the pixel size of the reconstructed object is 4 times smaller than the pixel size of the sensor. In comparison with the wavelength the achieved super-resolution is upto two thirds of the wavelength.

The following further work is planned. First, we are going to use a transition (not reflective) SLM, which allows to make propagation distance  $z$  much smaller and in this way to fulfill the condition Eq. (10). Second, we are going to use in our experiments a physical phase test-object, what will allow to observe details with the resolution smaller than the SLM's pixel size. Third, in the algorithm development, an adaptive correction of the transfer function for wavefront propagation will be

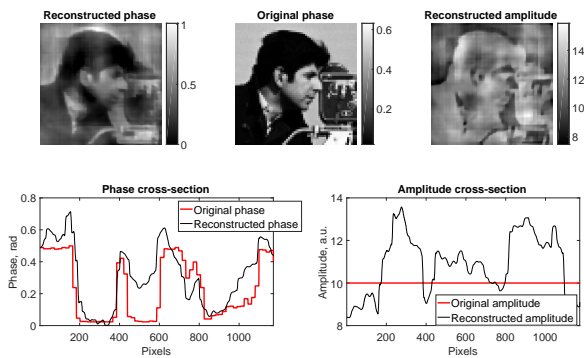


**Fig. 13.** Reconstructions for experimental data, phase object "cameraman", *subpixel super-resolution*. Top line, phases: reconstructed and original, left and middle images, respectively, and reconstructed amplitude –right image. Bottom line - phase (left) and amplitude (right) longitudinal cross-sections.

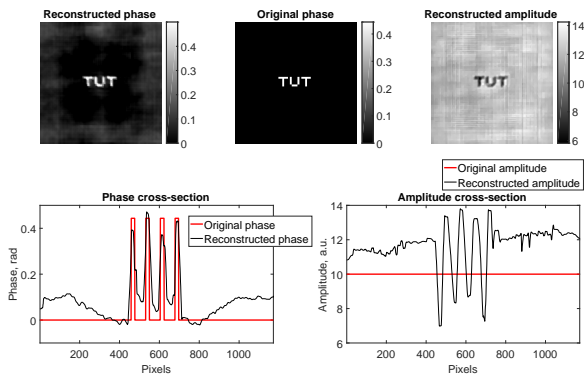


**Fig. 14.** Reconstructions for experimental data, phase object logo "TUT", *subpixel super-resolution*. Top line, phases: reconstructed and original, left and middle images, respectively, and reconstructed amplitude –right image. Bottom line - phase (left) and amplitude (right) longitudinal cross-sections.

designed.

## FUNDING

This work is supported by Academy of Finland, project no. 287150, 2015-2019, Russian Ministry of Education and Science (project within the state mission for institutions of higher education, agreement 3.1893.2017/PP) and Horizon 2020 TWINN-2015, grant 687328 - HOLO.

## REFERENCES

1. R. K. Tyson, "Principles of Adaptive Optics", 4rd ed., CRC Press (2014).
2. L. Wang and H. Wu, "Biomedical Optics: Principles and Imaging," John Wiley & Sons, Inc. (2007).
3. B. Kress and P. Meyrueis, "Applied Digital Optics: From Micro-Optics to Nanooptics," John Wiley & Sons Inc. (2009).
4. E. Can, and X. Li, M. Soltanolkotabi, "Phase Retrieval from Coded Diffraction Patterns," *Appl. Comput. Harmonic Anal.*, **39**, 177–299 (2015).
5. D. L. Misell, "An examination of an iterative method for the solution of the phase problem in optics and electron optics: I. Test calculations," *J. Phys. D Appl. Phys.* **6**, 2200–2216 (1973).
6. W. O. Saxton, "Correction of artefacts in linear and non-linear high resolution electron micrographs," *J. Microsc. Spectrosc. Electron.* **5**, 661–670 (1980).
7. G. Pedrini, W. Osten, and Y. Zhang, "Wave-front reconstruction from a sequence of interferograms recorded at different planes," *Opt. Lett.* **30**, 833-835 (2005).
8. P. Almero, G. Pedrini and W. Osten, "Complete wavefront reconstruction using sequential intensity measurements of a volume speckle field," *Appl. Opt.* **45**, 8596-8605 (2006).
9. P. Almero, A. M. S. Maallo, and S. Hanson, "Fast-convergent algorithm for speckle-based phase retrieval and a design for dynamic wavefront sensing," *Appl. Opt.* **48**, 1485-1493 (2009).
10. C. Kohler, F. Zhang, and W. Osten, "Characterization of a spatial light modulator and its application in phase retrieval," *Appl. Opt.* **48**, 4003–4008 (2009).
11. L. Camacho, V. Micy, Z. Zalevsky, and J. Garcha, "Quantitative phase microscopy using defocussing by means of a spatial light modulator," *Opt. Express* **18**, 6755–6766 (2010).
12. P. Almero, G. Pedrini, P. N. Gundu, W. Osten, S. G. Hanson, "Enhanced wavefront reconstruction by random phase modulation with a phase diffuser," *Opt. Laser. Eng.* **49**, 252-257 (2011).
13. E. J. Candès, X. Li, M. Soltanolkotabi, "Phase retrieval from coded diffraction patterns," *Appl. and Comp. Harm. Anal.* **9**, 277–299 (2015).
14. P. Almero, D. P. Quang Duc, I. Serrano-Garcia David, H. Satoshi, H. Yoshio, T. Mitsuo, and Y. Toyohiko, "Enhanced intensity variation for multiple-plane phase retrieval using spatial light modulator as convenient tunable diffuser," *Opt. Lett.* **41**, 2161-2164 (2016).
15. J. W. Goodman, *Introduction to Fourier optics*, 3rd Ed. Roberts & Company, Englewood, (2005).
16. R. W. Gerchberg and W. O. Saxton, "A practical algorithm for the determination of phase from image and diffraction plane pictures," *Optik* **35**, 237–246 (1972).
17. J. R. Fienup, "Phase retrieval algorithms: a comparison," *Appl. Opt.* **21**, 2758–2769 (1982).
18. C. Guo, S. Liu, Shi, J. T. Sheridan, "Iterative phase retrieval algorithms. I: optimization," *Appl. Opt.* **54**, 4698-4708 (2015).
19. Y. Shechtman, Y. C. Eldar, O. Cohen, H. N. Chapman, J. Miao, and M. Segev, "Phase retrieval with application to optical imaging: a contemporary overview," *IEEE Signal Process. Mag.* 87-109 (2015).
20. E. J. Candès, X. Li and M. Soltanolkotabi, "Phase retrieval via Wirtinger flow: theory and algorithms," *IEEE Trans. Inf. Theory*, **61**, 1985–2007 (2015).
21. Y. Chen and E. J. Candès, "Solving random quadratic systems of equations is nearly as easy as solving linear systems," <http://statweb.stanford.edu/~candes/papers/TruncatedWF.pdf> (2015).
22. V. Katkovnik, "Phase retrieval from noisy data based on sparse approximation of object phase and amplitude," [http://www.cs.tut.fi/~lasip/DDT/pdfs/Single\\_column.pdf](http://www.cs.tut.fi/~lasip/DDT/pdfs/Single_column.pdf) (2015).
23. Q. Lian, B. Shi, S. Chen, "Transfer orthogonal sparsifying

- transform learning for phase retrieval," *Digit Signal Process.* **62**, 11–25 (2017).
24. A. Fannjiang, "Absolute uniqueness of phase retrieval with random illumination," *Inverse Probl.* **28**, 075008 (2012).
  25. W. Bishara, U. Sikora, O. Mudanyali, T. W. Su, O. Yaglidere, S. Luckhart, and A. Ozcan, "Holographic pixel super-resolution in portable lensless on-chip microscopy using a fiber-optic array," *Lab Chip* **11**, 1276–1279 (2011).
  26. K. Guo, S. Dong, P. Nanda, and G. Zheng, "Optimization of sampling pattern and the design of Fourier ptychographic illuminator," *Opt. Express* **23**, 6171–6180 (2015).
  27. A. Greenbaum, W. Luo, B. Khademhosseini, T. W. Su, A. F. Coskun and A. Ozcan "Increased space-bandwidth product in pixel super-resolved lensfree on-chip microscopy," *Sci. Rep.* **3**, 1717 (2013).
  28. S. Gazit, A. Szameit, Y. C. Eldar, M. Segev, "Super-resolution and reconstruction of sparse sub-wavelength images," *Optics Express* **17**, 23920-23946 (2009).
  29. J. Song, C. L. Swisher, H. Im, S. Jeong, D. Pathania, Y. Iwamoto, M. Pivovarov, R. Weissleder and H. Lee, "Sparsity-Based Pixel Super Resolution for Lens-Free Digital In-line Holography," *Sci. Rep.* **6**, 24681 (2016).
  30. V. Katkovnik and K. Egiazarian, "Sparse super-resolution phase retrieval from phase-coded noisy intensity patterns," <http://www.cs.tut.fi/sgn/imaging/sparse/> (2017).
  31. V. Katkovnik and J. Astola, "High-accuracy wavefield reconstruction: decoupled inverse imaging with sparse modeling of phase and amplitude," *J. Opt. Soc. Am. A*, **29**, 44 – 54 (2012).
  32. V. Katkovnik and J. Astola, "Sparse ptychographical coherent diffractive imaging from noisy measurements," *J. Opt. Soc. Am. A* **30**, 367-379 (2013).
  33. K. Dabov, A. Foi, V. Katkovnik, and K. Egiazarian, "Image denoising by sparse 3D transform-domain collaborative filtering," *IEEE Trans. Image Process.* **16**, 2080-2095 (2007).
  34. A. Danielyan, V. Katkovnik, and K. Egiazarian, "BM3D frames and variational image deblurring," *IEEE Trans. Image Process.* **21**, 1715 – 1728 (2012).
  35. N. Verrier and M. Atlan, "Off-axis digital hologram reconstruction: some practical considerations," *Appl. opt.* **50**, H136–H146 (2011).
  36. F. Zhang, G. Pedrini, W. Osten, "Reconstruction algorithm for high-numerical-aperture holograms with diffraction-limited resolution", *Opt. Lett.* **31**, 1633–1635 (2006).
  37. N. Petrov, V. Bespalov, and M. Volkov, "Phase retrieval of THz radiation using set of 2D spatial intensity measurements with different wavelengths," *SPIE OPTO*, 82810J–82810J (2012).
  38. J. M. Bioucas-Dias and G. Valadão, "Phase unwrapping via graph cuts," *IEEE Trans. Image Process.* **16**, 698–709 (2007).
  39. P. Gemayel, B. Colicchio, A. Dieterlen, P. Ambs, "Cross-talk compensation of a spatial light modulator for iterative phase retrieval applications," *Appl. Opt.* **55**, 802-810 (2016).